Cell Reports
Physical Science

CellPress
OPEN ACCESS

Article

Catalytic hydrocracking of synthetic polymers into grid-compatible gas streams

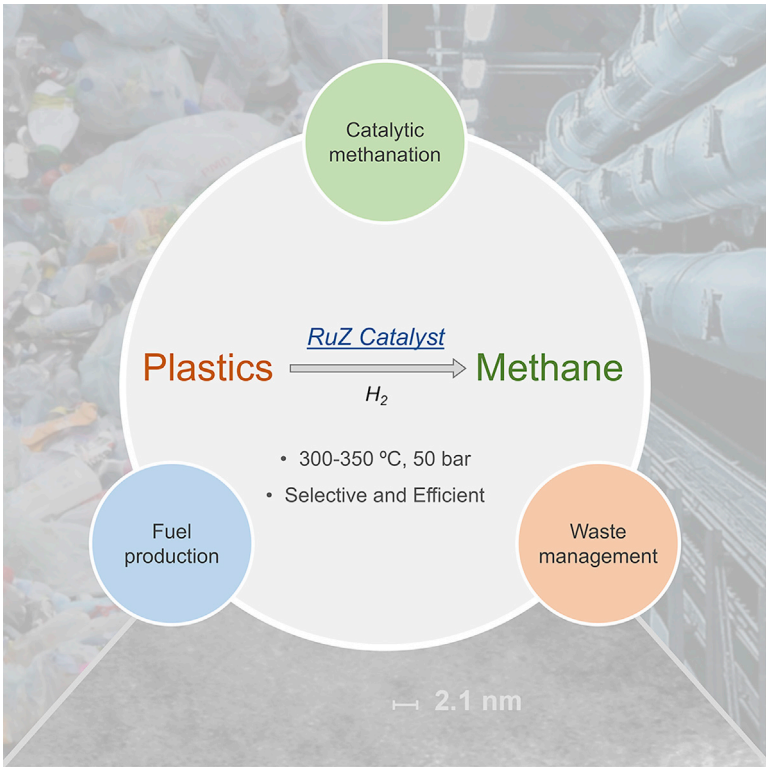

Lee et al. develop a Ru-modified zeolite catalyst for hydrocracking that converts various plastic materials selectively into methane. Characterization of the catalyst combined with experimental and computational studies provide insights into the reaction mechanism.

Wei-Tse Lee, Felix D. Bobbink, Antoine P. van Muyden, Kun-Han Lin, Clémence Corminboeuf, Reza R. Zamani, Paul J. Dyson

paul.dyson@epfl.ch

HIGHLIGHTS

Ru-modified zeolites efficiently catalyze the methanation of plastic materials

Outstanding selectivity toward methane can be achieved

Mechanistic studies reveal that the transformation occurs via chain end initiation

Evidence suggests a Ru-dominated reaction pathway

Lee et al., Cell Reports Physical Science 2, 100332
February 24, 2021
https://doi.org/10.1016/j.xcrp.2021.100332

Cell Reports
Physical Science

CellPress
OPEN ACCESS

Article

Catalytic hydrocracking of synthetic polymers into grid-compatible gas streams

Wei-Tse Lee,[1] Felix D. Bobbink,[1] Antoine P. van Muyden,[1] Kun-Han Lin,[1] Clémence Corminboeuf,[1] Reza R. Zamani,[2] and Paul J. Dyson[1,3,*]

SUMMARY

The use of methane as one of the cleanest energy sources has attracted significant public awareness, and methane production processes with less environmental impact than fracking are receiving considerable attention. Catalytic hydrocracking of plastic materials has been considered a potential clean alternative. However, catalysts that convert heterogeneous plastic feeds into a single product under industrially relevant conditions are lacking. Here, we describe a Ru-modified zeolite that catalytically transforms polyethylene, polypropylene, and polystyrene into grid-compatible methane (>97% purity), at 300°C–350°C using near-stoichiometric amounts of H_2. Mechanistic studies reveal a chain-end initiation process with limited isomerization of plastic substrates. A Ru site-dominant mechanism is proposed based on these studies and density functional theory (DFT) computations. We foresee that such a plastic-to-methane process may increase the intelligent use of plastic waste via energy recovery. There is also the potential to accommodate emerging sustainable H_2 production into existing natural gas networks, while integrating waste management, fuel production, and energy storage.

INTRODUCTION

The demand for methane, as one of the cleanest burning fuels, has increased drastically worldwide, with 4.6% growth in 2018 and 1.6% annual forecasting increment to 2024.[1] In addition, methane is a key platform chemical used to make a range of hydrocarbons, including virgin plastics.[2,3] Methane production from biomass or waste streams are attracting considerable public awareness recently.[4–6] Compared to typical methane production from fracking, both biomass and waste stream-derived production generate significantly fewer uncontrollable methane emissions into the atmosphere, resulting in fewer effects on the environment.[7] These production approaches also mitigate the pressures of current waste management facilities, particularly for waste plastic stream.

Over the years, global plastic production has increased, from 4 Mtons in 1955 to 407 Mtons in 2015, and it continues to increase (see Figure S1).[8] Of the 407 Mtons of plastics produced in 2015, only 11% were recycled (45 Mtons), with 14% incinerated (60 Mtons) and the remaining 75% (302 Mtons) untreated and either discarded in the environment or landfilled. The enormous quantities of plastics produced each year, combined with inadequate waste management, has led to a major environmental issue.[9]

Plastic streams are an intrinsically more efficient feed for methane transformation than biomass counterparts, and the direct conversion of carbon dioxide via the Sabatier reaction[10] as the C:H and C:O ratios are better matched with the target molecule (see Table S1). However, the majority of post-consumer plastic waste contains various plastic

[1]Institute of Chemical Sciences and Engineering, École Polytechnique Fédérale de Lausanne (EPFL), Lausanne, Switzerland

[2]Interdisciplinary Centre for Electron Microscopy, École Polytechnique Fédérale de Lausanne (EPFL), Lausanne, Switzerland

[3]Lead contact

*Correspondence: paul.dyson@epfl.ch

https://doi.org/10.1016/j.xcrp.2021.100332

materials and organic residues.[11,12] Consequently, landfill[13,14] and incineration[15] are used overwhelmingly to deal with heterogeneous plastic waste streams.

Elaborated waste management via chemical recycling for chemical and/or fuel recovery,[16–18] including pyrolysis,[19] gasification (thermal decomposition under controlled air flow for syngas production),[20,21] and hydrocracking,[22–24] has attracted significant attention. Nevertheless, pyrolysis and gasification usually result in a wide product distribution, including gases, liquids, and solid residuals (coke and ashes). Additional refinement and purification of the recovered liquid fuels or syngas transformations are required before their use.[25,26] In contrast, the hydrocracking of plastic feed as a reductive process tends to result in fewer undesirable products and is especially interesting if a single product can be obtained.

Taking Switzerland as an example, bio-based methane supplied <1% of the entire gas consumption in 2018, and >99% of the consumed methane was imported (325 GWh bio-methane versus 33,197 GWh imported).[27] Methane production via hydrocracking, valorizing <3% of the waste plastic stream (125 kg annual plastic waste per capita),[28] however, would be able to supply more than the current level of bio-methane (this value takes into account that 26% of plastic waste was recycled via other approaches in Switzerland).[29] A power-to-methane process[30,31] also enables the integration of emerging local sustainable H_2production into the existing natural gas infrastructure,[32] bridging waste management to energy storage across borders (note that a high H_2 content gas stream is unsuited to current ubiquitous gas grids, storage tanks, gas carriers, and so forth).[33]

Various catalysts have been shown to facilitate the hydrocracking of plastics. For example, zeolites were used to convert mixed pure plastics, polyethylene (PE) + polypropylene (PP) + polystyrene (PS), into liquid fuels, although the catalytic process does not significantly outperform thermal cracking performed at 400°C (see Figure S2A).[34] Consequently, transition metal nanoparticles (NPs) immobilized on amorphous silica-alumina or zeolites have been evaluated,[22,34–37] and Ni-modified mesoporous zeolites were shown to afford slightly reduced product distributions compared to thermal cracking when using PE as the feed (see Figure S2B).[22] However, none of the reactions delivered efficient transformation to methane.

Here, we report a selective hydrocracking process that transforms various plastics into methane in near-quantitative yield—in other words, a universal methanation process using all of the C fractions and suitable for direct injection into natural gas networks, using a catalyst designed for this application. Ru was used as it is superior to Ni in hydrocracking reactions, and although other noble metals may exhibit similar activity to that of Ru,[38] they are more expensive. The selectivity toward methane production is, to the best of our knowledge, unprecedented under relatively mild conditions (i.e., T [temperature] 350°C–440°C, P_{total} 60–100 bar, $P_{hydrogen}$ 20–55 bar)[39] and outperforms other reported catalysts.[40,41] Mechanistic studies show that the catalyst, composed of Ru NPs immobilized on a zeolite, operates via a different (Ru-dominant) mechanism to the general bifunctional (acid site and metal site) mechanism[42,43] usually observed for C–C bond hydrogenolysis.

RESULTS AND DISCUSSION

Catalyst optimization

A series of catalysts were prepared via a solution-based synthetic approach with Ru loadings ranging from 0.1 to 35 wt% (see Experimental procedures for further

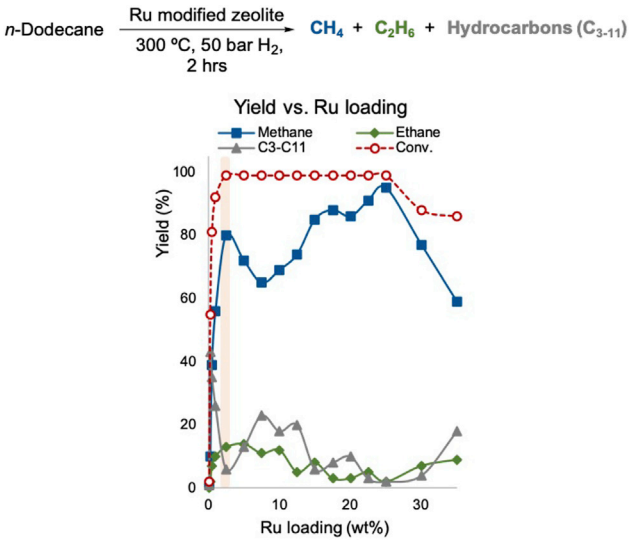

Figure 1. Ru loading versus conversion

Reaction conditions: *n*-dodecane (1.703 g, 10 mmol), Ru-modified zeolite (0.100–0.135 g, the applied weight of Ru catalyst depends on metal loading; see Table S2); 50 bar H_2 is 1.25 equiv. of the stoichiometric amount, applied for achieving full conversion under a higher reaction rate (a complete methane conversion is feasible under quantitative H_2, yet with lower kinetics; data not shown). The influence of the reaction pressure and temperature was also studied. See Note S1 and Figure S4. Note that both the zeolite solid support and the Ru precursor are unable to convert *n*-dodecane efficiently (1% and 4% conversion, respectively), indicating that a bifunctional mechanism does not lead to C–C bond cleavage, and hence cleavage is predominantly Ru site dominated. In general, a bifunctional mechanism takes place at higher temperatures than those used in our studies in other systems.[50,51] In addition, 5 wt% RuC was considerably less active (84% conversion). See Note S2 and Figure S5.

details).[44–47] The catalysts were then evaluated in the hydrocracking of *n*-dodecane, used as a model substrate representing the abundant PE plastics, with a substrate:-catalyst weight ratio of 16.5:1 at 300°C, under 50 bar H_2 for 2 h (Figure 1: 50 bar H_2 is slightly above the stoichiometric amount, see the legend for further details). The conversion increases rapidly from 2% at a Ru loading of 0.1 wt% to 97% at 2.5 wt % Ru loading, and remains at this level as the Ru loading increases to 25 wt%; but at higher Ru loadings, the conversion decreases. The selectivity to methane also increases with the Ru loading, with the yield reaching a local maximum of 79% at 2.5 wt % Ru, and at a Ru loading of 25 wt% the yield of methane peaks at 95% under the given conditions. The average Ru particle sizes were expected to increase with higher Ru loading. Transmission electron microscopy (TEM) images of the freshly prepared 25 wt% Ru loading catalyst demonstrated aggregated Ru clusters (~200 nm in diameter; Figure S3). Larger Ru clusters result in lower catalytic activity and less selectivity toward methane due to well-known size effects,[48,49] in accordance with varying ratios of particle surface area:volume. Consequently, the catalyst with a Ru loading of 2.5 wt%, called RuZ, was selected for further studies based on performance relative to cost (Figure 1; reactivity of RuZ is highlighted in amber).

Catalyst characterization

The powder X-ray diffraction (XRD) pattern of the untreated faujasite (FAU) zeolite is similar to that reported in the literature,[52] with the pattern of the RuZ catalyst being essentially unchanged with respect to that of the zeolite, indicating that the zeolite framework remains preserved in the RuZ catalyst (Figure 2A). The absence of additional peaks in the RuZ catalyst suggests that the Ru is well dispersed. As the Ru

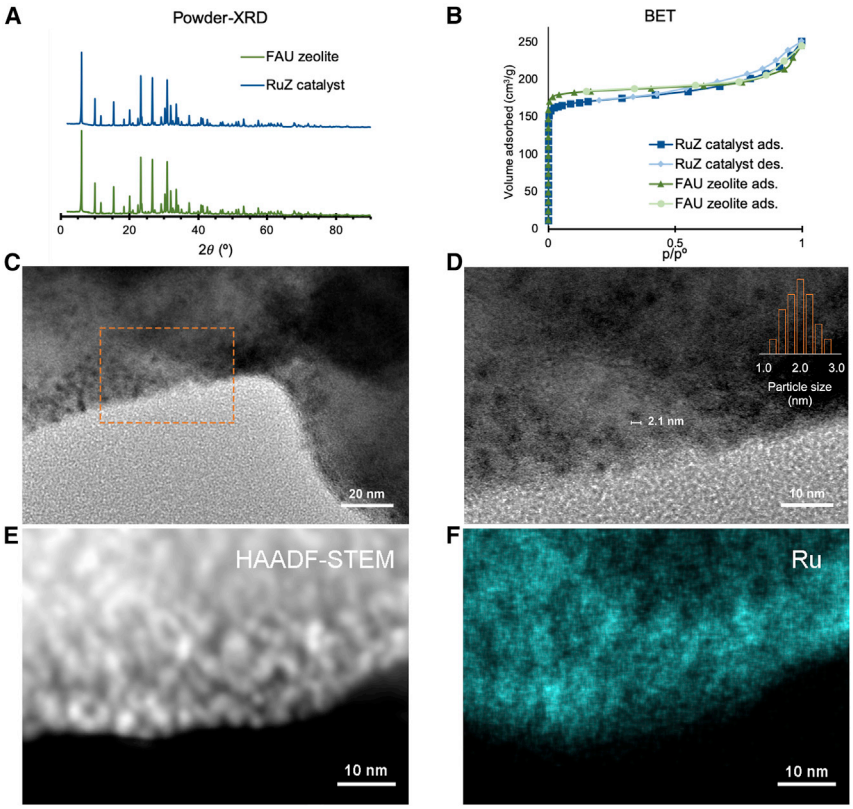

Figure 2. Characterizations of the RuZ catalyst

(A) Powder XRD.

(B) BET analysis (ads., adsorption; des., desorption).

(C) Bright-field (BF) TEM image (scale bar: 20 nm).

(D) Magnified BF TEM image of the orange-marked area with the Ru particle distribution (scale bar: 20 nm).

(E) High-angle annular dark-field (HAADF)-STEM image (scale bar: 10 nm).

(F) STEM-EDS elemental mapping of Ru (scale bar: 10 nm).

loading increases, the XRD patterns progressively change and the characteristic peaks of the zeolite become less intense (see Figure S6).

The porosity of the catalysts was determined by Brunauer-Emmett-Teller (BET) analysis (Figure 2B). The zeolite has a surface area of 852.49 $\pm$ 73.53 m^2/g and that of the RuZ catalysts is reduced to 737.56 $\pm$ 54.37 m^2/g as would be expected following the incorporation of Ru NPs (see Figure S7). TEM images and scanning TEM- energy-dispersive X-ray spectroscopy (STEM-EDS) mapping of the RuZ catalyst reveals that Ru NPs with diameters of ~2.1 $\pm$ 0.4 nm are embedded within the zeolite (Figures 2C–2F).

X-ray photoelectron spectroscopy (XPS) analysis shows that the major surface components in the RuZ catalyst are O, Si, and Al (66.8%, 16.6%, and 6.4%, respectively), with 1.7% surface Ru. The remaining surface elemental composition comprises Na, Mg, and Ca (ions) associated with the native zeolite aluminosilicate structure. The surface Ru concentration increases with the Ru loading, reaching a maximum value of 7.4% for the catalyst with a 30 wt% Ru loading (see Table S3 for further details). Ru (3p3/2) signals were applied for characterization to prevent misattributing Ru (3d3/2) and C (1 s) signals due to possible impurities typically found at ~284 eV. Fitting the Ru (3p3/2) signal indicates that the surface Ru is mostly present as RuO_2 (463.38 eV)[53]

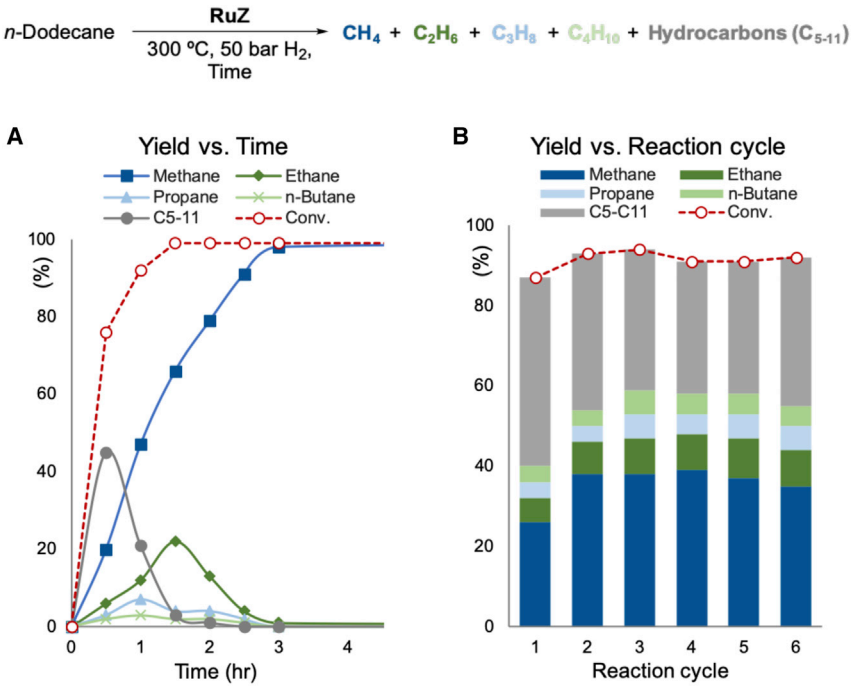

Figure 3. Kinetics and recycling for the methanation of *n*-dodecane using the RuZ catalyst
Reaction conditions: *n*-dodecane (1.703 g, 10 mmol) and RuZ (0.103 g) under batch conditions. Note that the differences in the yields for the recycling experiments compared to the other experiments are due to different experimental setups, see Supplemental information for further details.
(A) Kinetic trace.
(B) Recycling (reaction time = 2 h).

and RuO_x/Ru (465.17 eV),[54] and to a lesser extent as Ru/RuOx (462.05 eV)[54,55] (see Figures S8–S10). XPS of the RuZ catalyst was conducted in a resting state, and the oxidized Ru species are expected to be reduced into Ru metal under the reaction conditions (300°C, 50 bar H_2; see Methanation mechanism for further details).

Kinetic studies and recycling experiments

Kinetic plots obtained, with a substrate:catalyst weight ratio of 16.5:1, 300°C, and 50 bar H_2, for the methanation of *n*-dodecane reveal rapid conversion with >75% converted within 0.5 h and quantitatively conversion observed after 1.5 h (Figure 3A). The yield of methane reaches 20% after 0.5 h and 66% at 1.5 h, and after 3 h, the yield of methane is near quantitative. Recycling experiments involving 6 reaction cycles show that the catalyst is stable, with essentially no deterioration observed (Figure 3B; note that these studies were performed under sub-optimal conditions for representative recycling tests).[56] The slightly higher activity observed in the second cycle is attributed to the reduction of the surface Ru species in the first cycle, presumably an *in situ* activation step that takes place under the reductive operating condition. Thermogravimetric analysis (TGA) indicates that C deposition on the used RuZ catalyst does not take place (see Figure S11). In addition, STEM images of a used catalyst revealed no apparent aggregation of the Ru NPs (see Figure S12).

Methanation of plastic materials

Methanation of low-density polyethylene (LDPE) and PP was evaluated using the RuZ catalyst at 300°C, 50 bar H_2 (Figure 4A). Commercially available plastic materials (see Experimental procedures for further details) were selected to represent the abundant

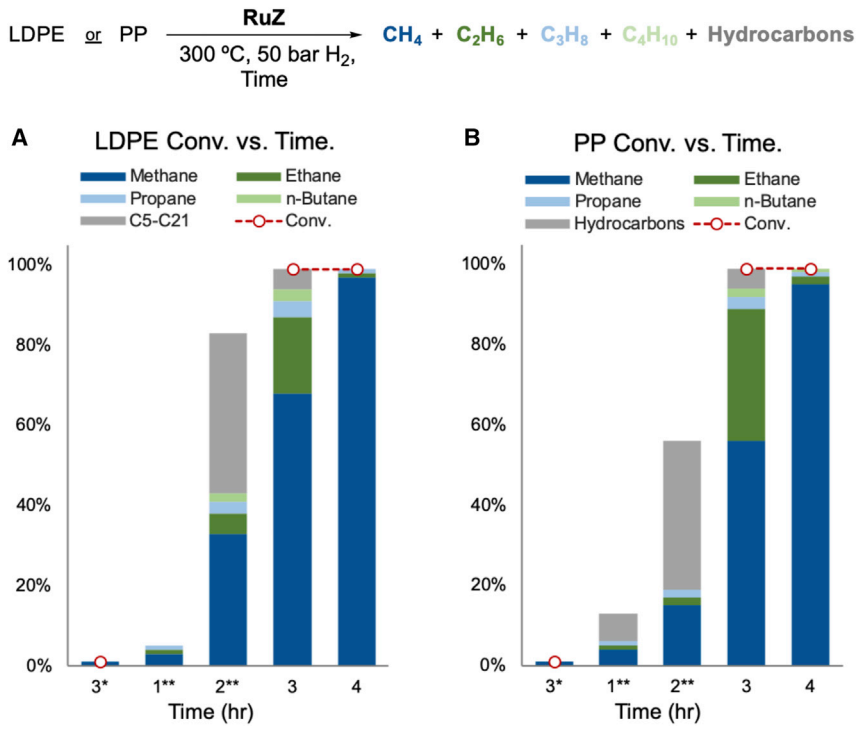

Figure 4. Methanation of plastics

Reaction conditions: RuZ (0.103 g). *Without RuZ catalyst. **-The conversion was not determined at 1 and 2 h (see supplemental experimental procedures for further details).

(A) LDPE (1.708 g, 61 mmol, based on monomer MW).

(B) PP (1.709 g, 41 mmol, based on monomer MW).

substrates of a possible waste stream. LDPE was quantitatively converted after 3 h, affording 96% gas products (C_{1-4}), with methane obtained in a 68% yield. The yield of methane increases to 97% after 4 h. Similarly, the yield of methane reached 95% after 4 h in the reaction involving PP (Figure 4B). Control experiments confirmed that the methanation of these plastics only takes place in the presence of the RuZ catalyst (Figures 4A and 4B).

At 350°C, PS is converted into methane in a 92% yield after 4 h (Table 1, entry 1). The higher temperature is required to prevent a semi-molten plastic layer coating the catalyst (typical PS melting point ~240°C), which hinders mass transfer (Table 1, entry 2). Mixed plastics (i.e., LDPE + PP + PS, 40:40:20 wt%), which simulate typical mixed plastic waste, were converted into methane in a near-quantitative yield after 4 h at 350°C (Table 1, entry 3).

Methanation mechanism

The generally accepted mechanism for alkane hydrogenolysis relies on a synergy between acid sites and metal sites present on supported metal catalysts (Figure 5A).[42] The acid sites are responsible for cracking/isomerizing the polymer, shortening the C chain, and affording unsaturated alkenes, which under the reductive environment are hydrogenated/dehydrogenated by the metal sites. However, under the conditions used with the RuZ catalyst, isomerized alkanes (C_{5-11}) were not observed and only traces of isomerized hydrocarbons (C_{5-21}) were identified during the methanation of *n*-dodecane and PE (see Figures S13 and S14 and Tables S4 and S5). These observations imply that the transformation takes place via a different mechanism. Moreover, a clear pattern of chain-end initiation to shorter hydrocarbons is observed and terminal C_1 species are

Table 1. Methanation of PS and mixed plastics

Entry	Substrate	Temp.(°C)	Conv. (%)	CH_4 (%)	C_2H_6 (%)	C_3H_8 (%)	Solid residues
1[a]	PS	350	>99	92	4	2	–
2[a]	PS	300	<10	1	0	0	✓
3[b]	LDPE + PP + PS	350	>99	99	0	0	–

Reaction conditions: H_2 (50 bar), 4 h.
[a]PS (0.780 g, 7.5 mmol, based on monomer MW) and RuZ (0.052 g).
[b]LDPE (0.672 g, 24 mmol), PP (0.672 g, 16 mmol), PS (0.312 g, 3 mmol), and RuZ (0.103 g).

unfavored in classical bifunctional mechanisms. A control experiment using 2-methylnonane as a substrate revealed that the alkyl chain preferentially cleaves at the primary C-atom adjacent to a secondary C rather than to a tertiary C-atom (see Figure S15). The major products are 2-methyloctane together with shorter branched alkanes, with only traces of n-nonane and shorter linear alkanes observed (branched/linear alkanes > 10/1, see Figures S16 and S17 and Tables S6 and S7).

Under the reductive environment, the surface RuO_x sites are expected to largely transform into Ru(0001),[57,58] with the concomitant formation of surface-bound H atoms (Figure 5B).[59,60] In addition, the chain-end of a linear alkane (R-CH_3) undergoes chemisorption on the Ru surface to afford an absorbed alkyl chain and a surface H atom (step 1 in Figure 5B, ΔE_a = 0.637 eV in Figure 5C),[61,62] similar to that reported previously.[63] The energy profiles were obtained via density functional theory (DFT) modeling with a 6-layer 3 × 3 Ru surface supercell and propane as the representative linear alkane (see Supplemental experimental procedures). At the initial stage, C–H bond cleavage is considerably favored over C–C bond cleavage ($\Delta E_{a'}$ = 0.188 eV versus 0.923 eV), and the C–H bond cleaved intermediate has a significantly lower energy state (ΔE of intermediate [Int.] 6 versus Int. 9 in Figure 5C). The absorbed alkyl chain undergoes further dehydrogenation to form alkylidene species involving both the terminal and adjacent C atoms (step 2 in Figure 5B),[64] rendering cleavage of the terminal C–C bond feasible in ΔE_a (0.759 versus 0.657 eV) and competitive with further C–H bond scission (*cf.* Int. CH_3C + CH versus Int. CH_3CC + H in Figure 5D). In addition, the match in activation energy toward initial chemisorption rationalizes the feasibility of C–C bond cleavage when the H_2 content is low. Next, concerted C–C bond cleavage is expected to take place, resulting in methylidyne[65] and alkylidyne species (step 3 in Figure 5B; optimized geometries are provided in Figures 5E and 5F). The methylidyne and the shortened alkylidyne then undergo hydrogenation to afford methane and an alkane that is reduced in length by one C atom (step 4 in Figure 5B). Propagation of this mechanism ultimately leads to a near-quantitative yield of methane and is fully consistent with the kinetic data. The main role of the zeolite appears to be that it minimizes sintering of the Ru particles, sustaining excellent recyclability.[66] Although branched hydrocarbon substrates (e.g., PP) may provide extra steric hindrance during intermediate formations and a lower H_2 atmosphere may lead to a less optimized ratio of surface H_2 and C species as suggested by the relevant literature,[67,68] we expected the C–C bond cleavage to be continuously accomplished via a similar Ru-dominated mechanism, based on the control studies (Figure S5).

Here, we report a Ru catalyst that efficiently transforms polyolefins and aromatic polymers into methane in near-quantitative yield under industrially relevant conditions, 300°C and 50 bar H_2. C–C bond cleavage operates via a Ru site-dominated mechanism on the Ru NPs, but not through a typical protonation/deprotonation step, taking place mainly on the acid sites. The resulting methane is sufficiently pure to allow direct injection into the existing natural gas networks. Even in the case of pursuing higher kinetics by applying excess reducing substrate, methane together with the slight H_2 residual are still qualified to be transported through the typical facilities

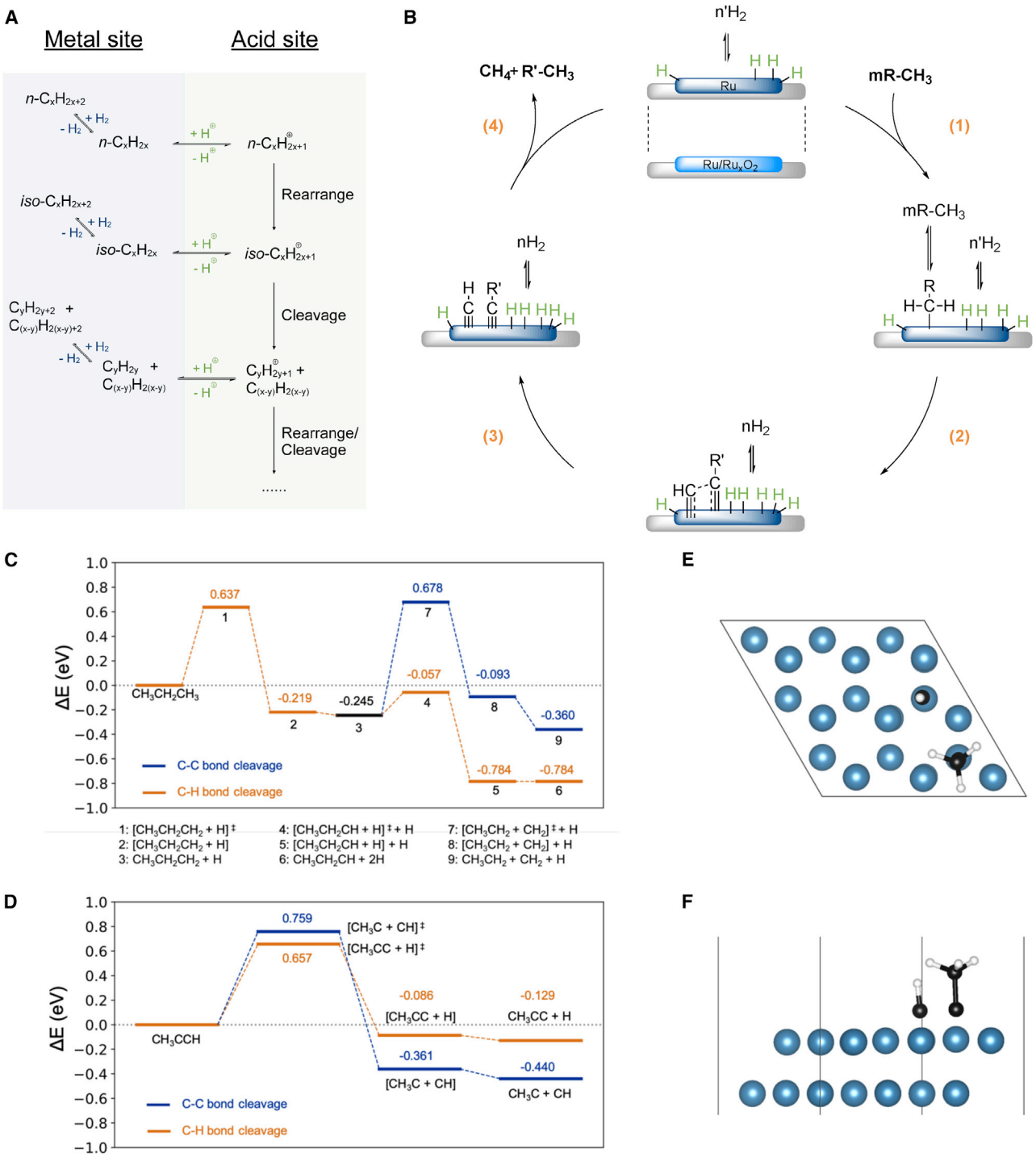

Figure 5. Mechanism inferences

(A) Bifunctional mechanism.

(B) Ru metal site-dominated methanation mechanism.

(C) DFT energy profile for the initial alkane chemisorption ([ ] represents the as-dissociated species; [ ]‡ represents the transition states; see Figure S18 and Table S8).

(D) DFT energy profile for C–C bond cleavage and C–H bond cleavage under low H_2-content conditions ([ ] represents the as-dissociated species; [ ]‡ represents the transition states; see Figure S19).

(E and F) Intermediate configurations after C–C bond cleavage. Top view (E) and side view (F); black: carbon, white: hydrogen, prussian: Ru; methylidyne: hcp site, alkylidyne: hcp site; see supplemental experimental procedures).

as a H_2-enriched nature gas (20 mol% of H_2) without further complications. This power-to-methane process paves a way to the integration of waste management with fuel production via synthetic methane and complements other approaches such as incineration when further coupled with sustainable hydrogen sources.

EXPERIMENTAL PROCEDURES

Resource availability

Lead contact

Further information and requests for resources should be directed to and will be fulfilled by the lead contact, Paul J. Dyson (paul.dyson@epfl.ch).

Materials availability

All unique reagents generated in this study are available from the lead contact on reasonable request.

Data and code availability

The data that support the plots and findings of this study are available from the lead contact on reasonable request.

General information

All of the experiments were reproduced at least 3 times to ensure reproducibility. Unless otherwise stated, all of the chemicals and materials were purchased and used without further purification. FAU zeolite and $RuCl_3 \cdot {}_3H_2O$ were purchased from ROTH and Precious Metals Online, respectively. *N*-Decane and *n*-dodecane were obtained from abcr GmbH. LDPE (melt index 25 g/10 min), PP (isostactic, average MW ~12,000), and PS (average MW ~35,000) were obtained from Sigma-Aldrich.

Synthesis of the catalysts

Commercial granules of FAU zeolite (10.0 g) were ground to a powder using a ceramic mortar. The powder was dispersed in deionized (DI) water (75.0 mL) in a round bottle flask (100 mL). The suspension was sonicated for 10 min and vacuum filtered. The residual solid FAU zeolite was washed with DI water (3 × 50.0 mL) and dried at 250°C in an oven for 18 h. In a typical procedure, $RuCl_3 \cdot 3H_2O$ (1.3–457.5 mg, 0.005–1.750 mmol) and the FAU zeolite (500 mg) were mixed with DI water (12.0 mL) in a round bottle flask (50 mL). The suspension was stirred (350 rpm) at 75°C for 1 h and cooled to room temperature. $NaBH_4$(s) (0.9–331 mg, 0.025–8.750 mmol) was dissolved in DI water (12.0 mL) and added to the suspension in 1 portion. The suspension was stirred (800 rpm) for 1 h. The resulting solid was vacuum filtered and washed by DI water (3 × 25 mL). The solid was then dried at 250°C in an oven for 18 h. Throughout our studies, different batches of the catalyst were prepared, characterized, and evaluated and were found to exhibit reproducible activities.

Typical procedure for *n*-dodecane methanation and Ru loading tests

n-Dodecane (1.703 g, 10.0 mmol) and Ru-modified zeolite (0.100–0.135 g, the applied weight of Ru catalyst depends on metal loading, see Table S2) were added to a glass vial (20 mL) with a glass magnetic stir, and the vial was then placed into an autoclave (75 mL, Parr Instrument). The autoclave was purged 3 times with H_2 and then pressurized to the appropriate pressure (50–100 bar) and sealed. The pressurized autoclave was placed in a heating block at the desired temperature (240°C–350°C) and stirred (500 rpm) for the given reaction time (1–18 h). After the reaction, the autoclave was cooled to room temperature in a water bath. The gaseous products were transferred into a balloon and injected into a specialized gas-sampling gas chromatograph/flame ionization detector (GC/FID) for analysis. For GC/mass spectrometry (MS) analysis of the liquid products,

p-xylene (0.106 g, 1 mmol) was added to the vial as an internal standard and analytical grade acetone was used as the solvent.

Typical procedure of plastic methanation

PE (1.700 g, based on monomer weight, 61 mmol) or PP (1.700 g, based on monomer weight, 40 mmol) and RuZ (0.103 mg) or PS (0.780 g, based on monomer weight, 7.5 mmol) and RuZ (0.052 g) were added to a glass vial (20 mL) with a glass magnetic stir, and the vial was then placed into an autoclave (75 mL, Parr Instrument). The autoclave was purged 3 times with H_2 and then pressurized to 50 bar. The pressurized autoclave was placed in a heating block at 300°C and stirred (500 rpm) for the given reaction time (1–18 h). After the reaction, the autoclave was cooled to room temperature in a water bath. The gaseous products were transferred into a balloon and injected into a specialized gas-sampling GC/FID for analysis. For GC/MS analysis of the liquid products, *p*-xylene (0.106 g, 1 mmol) was added to the vial as an internal standard and analytical grade acetone was used as the solvent. Note that the conversions were determined from the difference in the weight of the substrate before and after the reaction.

DFT computations

The Ru (0001) surface structure was constructed using a 6-layer 3 × 3 surface supercell with a 15-Å vacuum slab, reducing the interlayer interactions via periodic boundary conditions. Electronic structure computations and geometry optimization were performed via the Perdew-Burke-Ernzerhof (PBE) functional[69,70] along with the D3BJ correction.[71] A plane-wave basis with a kinetic energy cutoff of 400 eV was used to expand the electronic wavefunction. The 4 × 4 × 1 gamma-centered Monkhorst-Pack sampling method was used to generate an evenly spaced k-point grid. The valence electron and core interactions were described using the projector augmented wave (PAW) method.[72,73] The nudged elastic band (NEB) method[74] and the dimer method[75] were used in tandem for transition state optimizing. All of the computations were performed using the Vienna *ab initio* simulation package (VASP, version 5.4.4).[76–79]

SUPPLEMENTAL INFORMATION

Supplemental Information can be found online at https://doi.org/10.1016/j.xcrp.2021.100332.

ACKNOWLEDGMENTS

The studies are supported by the EPFL (Switzerland) and Swiss National Science Foundation. We thank Florent Héroguel, Pascal Schouwink, Pierre Mettraux, Yann Lavanchy, and Tzu-Hsien Shen for technical support.

AUTHOR CONTRIBUTIONS

All of the authors contributed to the design of the experiments and data analysis. W.-T.L. performed the experiments and K.-H.L. performed the DFT computations; W.-T.L. and P.J.D. wrote the manuscript; and all of the authors discussed, commented on, and proofread the manuscript.

DECLARATION OF INTERESTS

The catalyst is described in a patent invented by W.-T.L., F.D.B., A.P.v.M., and P.J.D. The other authors declare no competing interests.

Received: September 16, 2020
Revised: December 1, 2020
Accepted: January 12, 2021
Published: February 5, 2021

REFERENCES

1. International Energy Agency (2019). IEA Market Report Series: Gas 2019. https://webstore.iea.org/market-report-series-gas-2019.
2. Lašič Jurković, D., Puliyalil, H., Pohar, A., and Likozar, B. (2019). Plasma-activated methane partial oxidation reaction to oxygenate platform chemicals over Fe, Mo, Pd and zeolite catalysts. Int. J. Energy Res. *43*, 8085–8099.
3. Puliyalil, H., Lašič Jurković, D., Dasireddy, V.D.B.C., and Likozar, B. (2018). A review of plasma-assisted catalytic conversion of gaseous carbon dioxide and methane into value-added platform chemicals and fuels. RSC Adv. *8*, 27481–27508.
4. Chandra, R., Takeuchi, H., and Hasegawa, T. (2012). Methane production from lignocellulosic agricultural crop wastes: a review in context to second generation of biofuel production. Renew. Sustain. Energy Rev. *16*, 1462–1476.
5. Campuzano, R., and González-Martínez, S. (2016). Characteristics of the organic fraction of municipal solid waste and methane production: a review. Waste Manag. *54*, 3–12.
6. Rao, H., Schmidt, L.C., Bonin, J., and Robert, M. (2017). Visible-light-driven methane formation from CO_2 with a molecular iron catalyst. Nature *548*, 74–77.
7. Howarth, R.W., Ingraffea, A., and Engelder, T. (2011). Natural gas: should fracking stop? Nature *477*, 271–275.
8. Geyer, R., Jambeck, J.R., and Law, K.L. (2017). Production, use, and fate of all plastics ever made. Sci. Adv. *3*, e1700782.
9. Jambeck, J.R., Geyer, R., Wilcox, C., Siegler, T.R., Perryman, M., Andrady, A., Narayan, R., and Law, K.L. (2015). Plastic waste inputs from land into the ocean. Science *347*, 768–771.
10. Müller, K., Fleige, M., Rachow, F., and Schmeißer, D. (2013). Sabatier based CO2-methanation of flue gas emitted by conventional power plants. Energy Proc. *40*, 240–248.
11. Kalanatarifard, A., and Su Yang, G. (2012). Identification of the Municipal Solid Waste Characteristics and Potential of Plastic Recovery at Bakri Landfill, Muar, Malaysia. J. Sustain. Dev. *5*, 11–17.
12. Hargreaves, J.C., Adl, M.S., and Warman, P.R. (2008). A review of the use of composted municipal solid waste in agriculture. Agric. Ecosyst. Environ. *123*, 1–14.
13. Kaartinen, T., Sormunen, K., and Rintala, J. (2013). Case study on sampling, processing and characterization of landfilled municipal solid waste in the view of landfill mining. J. Clean. Prod. *55*, 56–66.
14. He, P., Chen, L., Shao, L., Zhang, H., and Lü, F. (2019). Municipal solid waste (MSW) landfill: a source of microplastics? Evidence of microplastics in landfill leachate. Water Res. *159*, 38–45.
15. Gradus, R.H.J.M., Nillesen, P.H.L., Dijkgraaf, E., and van Koppen, R.J. (2017). A Cost-effectiveness Analysis for Incineration or Recycling of Dutch Household Plastic Waste. Ecol. Econ. *135*, 22–28.
16. Rahimi, A., and García, J.M. (2017). Chemical recycling of waste plastics for new materials production. Nat. Rev. Chem. *1*, 0046.
17. Ragaert, K., Delva, L., and Van Geem, K. (2017). Mechanical and chemical recycling of solid plastic waste. Waste Manag. *69*, 24–58.
18. Jing, Y., Wang, Y., Furukawa, S., Xia, J., Sun, C., Hülsey, M.J., Wang, H., Guo, Y., Liu, X., and Yan, N. (2020). Towards the circular economy: converting aromatic plastic waste back to arenes over Ru/Nb2O5 catalyst. Angew. Chemie Int. Ed. Engl. https://doi.org/10.1002/anie.202011063.
19. Chen, D., Yin, L., Wang, H., and He, P. (2014). Pyrolysis technologies for municipal solid waste: a review. Waste Manag. *34*, 2466–2486.
20. Lopez, G., Artetxe, M., Amutio, M., Alvarez, J., Bilbao, J., and Olazar, M. (2018). Recent advances in the gasification of waste plastics. A critical overview. Renew. Sustain. Energy Rev. *82*, 576–596.
21. Wu, C., and Williams, P.T. (2010). Pyrolysis-gasification of plastics, mixed plastics and real-world plastic waste with and without Ni-Mg-Al catalyst. Fuel *89*, 3022–3032.
22. Escola, J.M., Aguado, J., Serrano, D.P., García, A., Peral, A., Briones, L., Calvo, R., and Fernandez, E. (2011). Catalytic hydroreforming of the polyethylene thermal cracking oil over Ni supported hierarchical zeolites and mesostructured aluminosilicates. Appl. Catal. B *106*, 405–415.
23. Escola, J.M., Aguado, J., Serrano, D.P., Briones, L., Díaz De Tuesta, J.L., Calvo, R., and Fernandez, E. (2012). Conversion of polyethylene into transportation fuels by the combination of thermal cracking and catalytic hydroreforming over Ni-supported hierarchical beta zeolite. Energy Fuels *26*, 3187–3195.
24. Munir, D., Irfan, M.F., and Usman, M.R. (2018). Hydrocracking of virgin and waste plastics: a detailed review. Renew. Sustain. Energy Rev. *90*, 490–515.
25. French, R.J., Hrdlicka, J., and Baldwin, R. (2010). Mild hydrotreating of biomass pyrolysis oils to produce a suitable refinery feedstock. Environ. Prog. Sustain. Energy *29*, 142–150.
26. de Miguel Mercader, F., Groeneveld, M.J., Kersten, S.R.A., Way, N.W.J., Schaverien, C.J., and Hogendoorn, J.A. (2010). Production of advanced biofuels: co-processing of upgraded pyrolysis oil in standard refinery units. Appl. Catal. B *96*, 57–66.
27. Swiss Federal Office of Energy (2019). Energy Consumption in Switzerland 2018 (Swiss Federal Office of Energy).
28. Federal Office for the Environment OFEN (2020). Plastics. https://www.bafu.admin.ch/bafu/en/home/topics/waste/guide-to-waste-a-z/plastics.html.
29. PlasticsEurope (2019). Plastics – the Facts 2019. https://www.plasticseurope.org/application/files/9715/7129/9584/FINAL_web_version_Plastics_the_facts2019_14102019.pdf.
30. Thema, M., Bauer, F., and Sterner, M. (2019). Power-to-Gas: electrolysis and methanation status review. Renew. Sustain. Energy Rev. *112*, 775–787.
31. Bailera, M., Lisbona, P., Romeo, L.M., and Espatolero, S. (2017). Power to Gas projects review: lab, pilot and demo plants for storing renewable energy and CO2. Renew. Sustain. Energy Rev. *69*, 292–312.
32. Jones, D.R., Al-Masry, W.A., and Dunnill, C.W. (2018). Hydrogen-enriched natural gas as a domestic fuel: an analysis based on flash-back and blow-off limits for domestic natural gas appliances within the UK. Sustain. Energy Fuels *2*, 710–723.
33. Melaina, M., Antonia, O., and Penev, M. (2013). Blending Hydrogen into Natural Gas Pipeline Networks: A Review of Key Issues. https://www.energy.gov/sites/prod/files/2014/03/f11/blending_h2_nat_gas_pipeline.pdf.
34. Munir, D., Abdullah, Piepenbreier, F., and Usman, M.R. (2017). Hydrocracking of a plastic mixture over various micro-mesoporous composite zeolites. Powder Technol. *316*, 542–550.
35. Serrano, D.P., Escola, J.M., Briones, L., Medina, S., and Martínez, A. (2015). Hydroreforming of the oils from LDPE thermal cracking over Ni–Ru and Ru supported over hierarchical beta zeolite. Fuel *144*, 287–294.
36. Castaño, P., Gutiérrez, A., Hita, I., Arandes, J.M., Aguayo, A.T., and Bilbao, J. (2012). Deactivating species deposited on Pt-Pd catalysts in the hydrocracking of light-cycle oil. Energy Fuels *26*, 1509–1519.
37. Martens, J.A., Verboekend, D., Thomas, K., Vanbutsele, G., Pérez-Ramírez, J., and Gilson, J.-P. (2013). Hydroisomerization and hydrocracking of linear and multibranched long model alkanes on hierarchical Pt/ZSM-22 zeolite. Catal. Today *218–219*, 135–142.
38. Kua, J., Faglioni, F., and Goddard, W.A. (2000). Thermochemistry for hydrocarbon intermediates chemisorbed on metal surfaces: CH(n-m)(CH3)(m) with n = 1, 2, 3 and m $\leq$ n on Pt, Ir, Os, Pd, Rh, and Ru. J. Am. Chem. Soc. *122*, 2309–2321.
39. Bricker, M., Thakkar, V., and Petri, J. (2015). Hydrocracking in petroleum processing. Handb. Pet. Process. *1*, 317–356.
40. Celik, G., Kennedy, R.M., Hackler, R.A., Ferrandon, M., Tennakoon, A., Patnaik, S., LaPointe, A.M., Ammal, S.C., Heyden, A., Perras, F.A., et al. (2019). Upcycling Single-Use Polyethylene into High-Quality Liquid Products. ACS Cent. Sci. *5*, 1795–1803.
41. Dufaud, V., and Basset, J.M. (1998). Catalytic hydrogenolysis at low temperature and pressure of polyethylene and polypropylene to diesels or lower alkanes by a zirconium hydride supported on silica-alumina: a step toward polyolefin degradation by the microscopic reverse of Ziegler-Natta polymerization. Angew. Chem. Int. Ed. Engl. *37*, 806–810.
42. Weitkamp, J. (2012). Catalytic Hydrocracking-Mechanisms and Versatility of the Process. ChemCatChem *4*, 292–306.

43. Akhmedov, V.M., and Al-Khowaiter, S.H. (2000). Hydroconversion of hydrocarbons over Ru-containing supported catalysts prepared by metal vapor method. Appl. Catal. A Gen. *197*, 201–212.

44. Eckle, S., Anfang, H.G., and Behm, R.J. (2011). Reaction intermediates and side products in the methanation of CO and CO2 over supported Ru catalysts in H2-rich reformate gases. J. Phys. Chem. C *115*, 1361–1367.

45. Luo, Z., Zheng, Z., Li, L., Cui, Y.-T., and Zhao, C. (2017). Bimetallic Ru−Ni Catalyzed Aqueous-Phase Guaiacol Hydrogenolysis at Low H 2 Pressures. ACS Catal. *7*, 8313.

46. Wang, F., He, S., Chen, H., Wang, B., Zheng, L., Wei, M., Evans, D.G., and Duan, X. (2016). Active Site Dependent Reaction Mechanism over Ru/CeO2 Catalyst toward CO2 Methanation. J. Am. Chem. Soc. *138*, 6298–6305.

47. Van den Bosch, S., Schutyser, W., Koelewijn, S.F., Renders, T., Courtin, C.M., and Sels, B.F. (2015). Tuning the lignin oil OH-content with Ru and Pd catalysts during lignin hydrogenolysis on birch wood. Chem. Commun. (Camb.) *51*, 13158–13161.

48. Gao, J., Jia, C., Zhang, M., Gu, F., Xu, G., and Su, F. (2013). Effect of nickel nanoparticle size in Ni/α-Al2O 3 on CO methanation reaction for the production of synthetic natural gas. Catal. Sci. Technol. *3*, 2009–2015.

49. Wang, S., Yin, K., Zhang, Y., and Liu, H. (2013). Glycerol hydrogenolysis to propylene glycol and ethylene glycol on zirconia supported noble metal catalysts. ACS Catal. *3*, 2112–2121.

50. García, R.A., Serrano, D.P., and Otero, D. (2005). Catalytic cracking of HDPE over hybrid zeolitic-mesoporous materials. J. Anal. Appl. Pyrolysis *74*, 379–386.

51. Corma, A., Miguel, P.J., and Orchillés, A.V. (1994). The Role of Reaction Temperature and Cracking Catalyst Characteristics in Determining the Relative Rates of Protolytic Cracking, Chain Propagation, and Hydrogen Transfer. J. Catal. *145*, 171–180.

52. Kita, H., Fuchida, K., Horita, T., Asamura, H., and Okamoto, K. (2001). Preparation of Faujasite membranes and their permeation properties. Separ. Purif. Tech. *25*, 261–268.

53. Folkesson, B., Bjorøy, M., Pappas, J., Skaarup, S., Aaltonen, R., and Swahn, C.-G. (1973). ESCA Studies on the Charge Distribution in Some Dinitrogen Complexes of Rhenium, Iridium, Ruthenium, and Osmium. Acta Chem. Scand. *27*, 287–302.

54. Shen, J.Y., Adnot, A., and Kaliaguine, S. (1991). An ESCA study of the interaction of oxygen with the surface of ruthenium. Appl. Surf. Sci. *51*, 47–60.

55. Thampi, K.R., Kiwi, J., and Grätzel, M. (1987). Methanation and photo-methanation of carbon dioxide at room temperature and atmospheric pressure. Nature *327*, 506–508.

56. Scott, S.L. (2018). A Matter of Life(time) and Death. ACS Catal. *8*, 8597–8599.

57. Jae, J., Zheng, W., Karim, A.M., Guo, W., Lobo, R.F., and Vlachos, D.G. (2014). The role of Ru and RuO2 in the catalytic transfer hydrogenation of 5-hydroxymethylfurfural for the production of 2,5-dimethylfuran. ChemCatChem *6*, 848–856.

58. Han, J.H., Lee, S.W., Kim, S.K., Han, S., Hwang, C.S., Dussarrat, C., and Gatineau, J. (2010). Growth of RuO2 thin films by pulsed-chemical vapor deposition using RuO4 precursor and 5% H2 reduction gas. Chem. Mater. *22*, 5700–5706.

59. Vincent, J.K., Olsen, R.A., Kroes, G.J., Luppi, M., and Baerends, E.J. (2005). Six-dimensional quantum dynamics of dissociative chemisorption of H2 on Ru(0001). J. Chem. Phys. *122*, 44701.

60. Groot, I.M.N., Ueta, H., van der Niet, M.J.T.C., Kleyn, A.W., and Juurlink, L.B.F. (2007). Supersonic molecular beam studies of dissociative adsorption of H2 on Ru(0001). J. Chem. Phys. *127*, 244701.

61. Ciobîcă, I.M., Frechard, F., Van Santen, R.A., Kleyn, A.W., and Hafner, J. (2000). A DFT Study of Transition States for C-H Activation on the Ru(0001) Surface. J. Phys. Chem. B *104*, 3364–3369.

62. Zaera, F. (2017). The Surface Chemistry of Metal-Based Hydrogenation Catalysis. ACS Catal. *7*, 4947–4967.

63. Ande, C.K., Elliott, S.D., and Kessels, W.M.M. (2014). First-principles investigation of C-H bond scission and formation reactions in ethane, ethene, and ethyne adsorbed on Ru(0001). J. Phys. Chem. C *118*, 26683–26694.

64. Yang, M.L., Zhu, Y.A., Fan, C., Sui, Z.J., Chen, D., and Zhou, X.G. (2011). DFT study of propane dehydrogenation on Pt catalyst: effects of step sites. Phys. Chem. Chem. Phys. *13*, 3257–3267.

65. Lenz-Solomun, P., Wu, M.C., and Goodman, D.W. (1994). Methane coupling at low temperatures on Ru(0001) and Ru(11-20) catalysts. Catal. Lett. *25*, 75–86.

66. Zhang, J., Wang, L., Zhang, B., Zhao, H., Kolb, U., Zhu, Y., Liu, L., Han, Y., Wang, G., Wang, C., et al. (2018). Sinter-resistant metal nanoparticle catalysts achieved by immobilization within zeolite crystals via seed-directed growth. Nat. Catal. *1*, 540–546.

67. Nakagawa, Y., Oya, S.I., Kanno, D., Nakaji, Y., Tamura, M., and Tomishige, K. (2017). Regioselectivity and Reaction Mechanism of Ru-Catalyzed Hydrogenolysis of Squalane and Model Alkanes. ChemSusChem *10*, 189–198.

68. Hibbitts, D.D., Flaherty, D.W., and Iglesia, E. (2016). Effects of Chain Length on the Mechanism and Rates of Metal-Catalyzed Hydrogenolysis of n-Alkanes. J. Phys. Chem. C *120*, 8125–8138.

69. Perdew, J.P., Burke, K., and Ernzerhof, M. (1996). Generalized gradient approximation made simple. Phys. Rev. Lett. *77*, 3865–3868.

70. Perdew, J.P., Burke, K., and Ernzerhof, M. (1997). Generalized Gradient Approximation Made Simple [erratum]. Phys. Rev. Lett. *78*, 1396.

71. Grimme, S., Ehrlich, S., and Goerigk, L. (2011). Effect of the damping function in dispersion corrected density functional theory. J. Comput. Chem. *32*, 1456–1465.

72. Joubert, D. (1999). From ultrasoft pseudopotentials to the projector augmented-wave method. Phys. Rev. B Condens. Matter Mater. Physiol. *59*, 1758–1775.

73. Blöchl, P.E. (1994). Projector augmented-wave method. Phys. Rev. B Condens. Matter *50*, 17953–17979.

74. Henkelman, G., Uberuaga, B.P., and Jónsson, H. (2000). Climbing image nudged elastic band method for finding saddle points and minimum energy paths. J. Chem. Phys. *113*, 9901–9904.

75. Henkelman, G., and Jónsson, H. (1999). A dimer method for finding saddle points on high dimensional potential surfaces using only first derivatives. J. Chem. Phys. *111*, 7010–7022.

76. Kresse, G., and Furthmüller, J. (1996). Efficient iterative schemes for ab initio total-energy calculations using a plane-wave basis set. Phys. Rev. B Condens. Matter *54*, 11169–11186.

77. Kresse, G., and Furthmüller, J. (1996). Efficiency of ab-initio total energy calculations for metals and semiconductors using a plane-wave basis set. Comput. Mater. Sci. *6*, 15–50.

78. Kresse, G., and Hafner, J. (1994). Ab initio molecular-dynamics simulation of the liquid-metal-amorphous-semiconductor transition in germanium. Phys. Rev. B Condens. Matter *49*, 14251–14269.

79. Kresse, G., and Hafner, J. (1993). Ab initio molecular dynamics for liquid metals. Phys. Rev. B Condens. Matter *47*, 558–561.